Planet. Space Sci., Vol. 24, pp. 975 to 985. Pergamon Press, 1976. Printed in Northern Ireland

ROTATING ION-EXOSPHERES

J. LEMAIRE
Aeronomy Institute, 3 avenue Circulaire, B-1180 Brussels, Belgium

(*Received* 1 *April* 1976)

Abstract—The density, parallel and perpendicular pressures and temperatures distributions of a collisionless thermal plasma trapped in a dipole magnetic field are described and discussed. The effect of rotation on the plasma distribution is illustrated. The relative population of the different types of trapped particles is shown to influence drastically the temperature anisotropy of the cold plasma in the ion-exosphere. The total contents of mass, potential energy and kinetic energy in the magnetic flux tubes are estimated.

1. INTRODUCTION

Since the mean free path (l) of thermal ions increases rapidly with altitude, there is usually an exobase level where l becomes larger than the density scale height. Above this altitude, in the exosphere, the Knudsen number of the plasma is larger than unity, and it is difficult to justify the validity of the Chapman–Enskog expansion (i.e. the Euler or the Navier–Stokes or the Burnett approximation closing up the general transport equations). Therefore it is worthwhile to describe the distribution of collisionless plasma in ion-exospheres from another point of view: the kinetic theory.

The simplest (and ideal) kinetic approximation is then to assume that above exobase the charged particles have no collisions and move unperturbed along a trajectory determined by their energy and pitch angle.

It is always possible to find an arbitrary function of the particle velocity which has the same M first order moments (density, fluxes, pressure tensors . . .) as the actual velocity distribution (Lemaire and Scherer, 1971, 1973b). This arbitrary function is then used as a boundary condition for Liouville or Vlasov equations to calculate the M first order moments (density, fluxes . . .) at any other point in the exosphere.

The kinetic theory has been used by Eviatar *et al.* (1964) and Hartle (1969) to determine the density and temperature distribution along closed magnetic field lines. It has also been used by Lemaire and Scherer (1970, 1971, 1973, 1974) to determine field aligned distributions of the multi-ionic polar wind, solar wind and auroral collisionless plasmas.

The purpose of this paper is to extend the exospheric models to take into account the effect of azimuthal rotation of the plasma on its distribution along a dipole magnetic field line. The distribution of thermal particles depends not only on the gravitational potential but also on the centrifugal potential which is described in Section 2. The different types of orbits of collisionless particles are discussed in Section 3. The density, pressure and temperature anisotropy of a hydrogen plasma in a rotating ion-exosphere are given in Sections 4 and 5. The total density, potential energy and kinetic energy in a flux tube are calculated in Section 5. The discussion of the effects of angular speed is given in Section 6. The conclusions are in Section 7.

2. THE DISTRIBUTION OF POTENTIAL ENERGY

Let us consider a fully-ionized hydrogen plasma drifting with an angular speed, Ω, around the axis of symmetry of a dipole magnetic field. In the frame of reference rotating with the plasma the gravitational and centrifugal potential energies of particles of mass m are respectively

$$m\phi_g = -\frac{GMm}{r} + Cst, \tag{1}$$

$$m\phi_\Omega = -\frac{1}{2} m\Omega^2 r^2 \cos^2 \lambda + Cst, \tag{2}$$

where M is the mass of the planet, G is the gravitational constant, r and λ are the radial distance and latitude of the particle.

The gravitational and centrifugal forces induce a charge separation electric field in the plasma (as a consequence of the difference in ion and electron masses). Under steady state conditions the electric field in the rotating frame of reference is given by

$$\mathbf{E} = -\nabla\phi_E(r, \lambda). \tag{3}$$

When the plasma is isothermal and in *hydrostatic*

barometric equilibrium, the quasi-neutrality condition implies that

$$\phi_E = -\frac{m_i T_e - m_e T_i}{e(T_i + T_e)}(\phi_g + \phi_\Omega) + Cst. \qquad (4)$$

This is known as the Pannekoek (1922)–Rosseland (1924) electrostatic potential distribution. With such an electric field the total potential energy is the same for an electron and an ion:

$$\left(\frac{m\phi_t}{T}\right)_e = \left(\frac{m\phi_t}{T}\right)_i = \frac{m_i + m_e}{T_i + T_e}(\phi_g + \phi_\Omega) + Cst. \qquad (5)$$

In a *collisionless ion-exosphere* where the density distribution can significantly depart from the barometric law the Pannekoek-Rosseland electric field and potential is not valid in general (see, Lemaire and Scherer, 1974). However, the Pannekoek-Rosseland polarization electric field remains applicable to a *single ion* plasma when there is *no net particle flux along the magnetic field line.* These conditions are fulfilled in the following models since we have considered a pure hydrogen plasma with symmetric exobase conditions in both hemispheres and consequently without net interhemisphere mass or heat flow. In the more complicated (and less ideal) case of *multi-ionic* collisionless plasma *with field aligned mass flow*, equation (4) is no longer valid and the electric potential must be found by solving the local quasi-neutrality condition for each altitude. Such a procedure has been introduced by Lemaire and Scherer (1969) in the case of a multi-ionic model of the polar wind.

The total potential energy (5) of a particle spiralling along dipole magnetic field lines is a function of the latitude λ, and is illustrated in Fig. 2 of Lemaire (1974) assuming corotation of the Earth plasmasphere. The Figs. 2 and 3 of Michel and Sturrock (1974) illustrate the meridional sections of the equipotential surfaces ($m\phi_t = Cst$) assuming corotation of Jupiter's and the Earth's plasmasphere.

Along a dipole magnetic field line with L larger than the critical value

$$L_c = \left(\frac{2}{3}\frac{GM}{\Omega^2 R^3}\right)^{1/3}, \qquad (6)$$

(R is the radius of the Planet) the total potential energy increases from zero at the exobase reference level (r_0) to a maximum value

$$m\phi_{t,M} = -\frac{m_i + m_e}{2}\frac{GM}{LR} \times \left[\frac{4}{3}\left(\frac{L}{L_c}\right)^{3/4} - \frac{LR}{r_0} - \frac{1}{3}\left(\frac{r_0}{L_c R}\right)^3\right] \qquad (7)$$

at the radial distance

$$r_M = LR\left(\frac{L_c}{L}\right)^{3/4}. \qquad (8)$$

For simplicity we assumed that $T_e = T_i = T_0$ in equation (5). Between r_M and $r_{eq} = LR$, ϕ_t is a decreasing function of the altitude, and has a minimum value in the equatorial plane,

$$m\phi_{t,eq} = -\frac{m_i + m_e}{2}\frac{GM}{LR} \times \left[1 + \frac{L^3}{3L_c^3} - \frac{LR}{r_0} - \frac{1}{3}\left(\frac{r_0}{L_c R}\right)^3\right]. \qquad (9)$$

The critical L-value (6) defines the equatorial distance of a surface which is called the Roche limit of ionospheric plasma confined in a dipole magnetic field. For field lines and plasma corotating with the Earth's angular velocity, ($\Omega_E = 7.29 \times 10^{-5}$ rad sec^{-1}, $L_c = 5.78$ (Lemaire, 1974); for $\Omega = 2\Omega_E$ the equation (6) gives $L_c \times 3.64$; for Jupiter, $L_c = 1.94$ if $\Omega = \Omega_J = 1.76 \times 10^{-4}$ rad sec^{-1} (Melrose, 1967; Michel and Sturrock, 1974); for $\Omega = 0.163\,\Omega_J$ one finds that $L_c = 6.5$.

Thus, as for a rotating stellar atmosphere, it is possible to define a Roche limit surface where the field aligned components of the gravitational force and the centrifugal force balance each other. This surface is also a locus of points where the barometric (hydrostatic) density distribution has a minimum value.

Beyond this surface the gas tends to move away from the Earth or to pile up in the equatorial potential well. Low energy particles (<1 eV for the Earth; <10 eV for Jupiter) can become trapped in this potential well. As will be discussed in the following section, this new class of trapped particles does not exist in the model of Eviatar *et al.* (1964) where it was assumed that $\Omega = 0$ and consequently $L_c = \infty$.

3. THE CLASSES OF PARTICLE ORBITS

Depending on their kinetic energy and pitch angle the orbits of particles moving along a magnetic field line in the potential field (5) can be organized into different classes.

3.1

For $L < L_c$, ϕ_t is a monotonic increasing function of altitude with a maximum at the equator, as in the case considered by Eviatar *et al.* (1964). Considering that the magnetic moment of the particles is conserved, one can define at any point A a loss

cone angle θ_A by

$$\sin^2\theta_A = \frac{B_A}{B_0}\frac{\frac{1}{2}mv^2 + m\phi_{t,A}}{\frac{1}{2}mv^2} \tag{10}$$

or

$$\sin^2\theta_A = \eta_A \frac{V^2+\psi_A}{V^2}, \tag{11}$$

where $\eta_A = B_A/B_0$, is the ratio of magnetic field intensity at the point A and at the exobase level (r_0) where the Coulomb collisions become unimportant; V is the dimensionless velocity of the particles ($V^2 = mv^2/2kT_0$, and T_0 is the exobase temperature); ψ_A is the dimensionless potential energy at the point $A(\psi_A = m\phi_{t,A}/kT_0)$.

Any particle whose pitch angle, θ, is smaller than θ_A or larger than $\pi - \theta_A$ has its mirror points in the collision dominated region below r_0. It belongs to the "ballistic" or "escaping" classes of particles which are illustrated by the shaded areas (b) and (e) in the panel A of Fig. 1. The central shaded area (b) of the velocity space ($V_\parallel$, $V_\perp$) corresponds to all the particles emerging from the ionosphere but which have not enough kinetic energy to reach the equatorial plane, and which fall back to the collision-dominated region. The outer shaded region (e) contains all the particles bouncing in the conjugate ionospheric region.

The particles with pitch angles outside the loss cone (i.e. $\theta_A < \theta < \pi - \theta_A$) have magnetic mirror points above the exobase. The trapped orbits are represented by the areas (t_1) and (t_2) in panel A of Fig. 1. The low energy trapped particles (t_1) have two reflection points in the same hemisphere, and the higher energy trapped particles (t_2) have magnetically conjugate mirror points in both hemispheres. Note that in the high energy limit ($: V^2 \gg \psi_A$), the loss cone angle is given by the familiar expression $\theta_A = \arcsin[(B_A/B)^{1/2}]$.

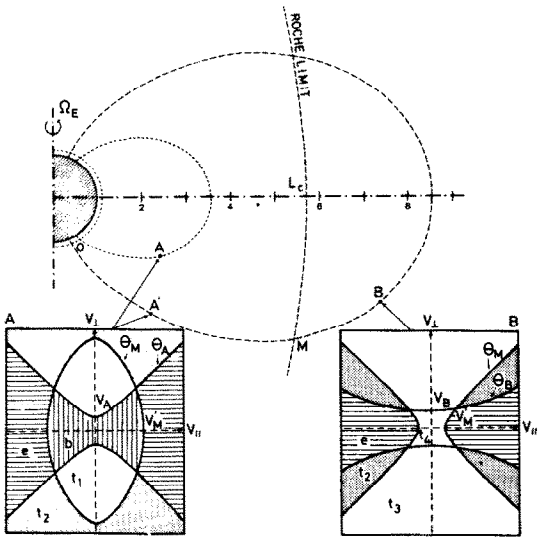

FIG. 1. CLASSES OF CHARGED PARTICLES IN A ROTATING ION-EXOSPHERE.

Panel A illustrates a section of the velocity space at a point below the Roche limit surface; Panel B, *ibid.* at a point above the Roche limit.

3.2

Let us now consider a field line $L(>L_c)$ crossing the Roche limit surface at the radial distance r_M given by equation (8). At any point $A'(r_{A'} < r_M)$ inside the Roche limit surface the orbits of particles can be organized in similar classes as discussed in Section 3.1 for the point A. The only difference is that the equatorial value of ψ(or $m\phi_t$) must be replaced by the maximum value ψ_M (or $m\phi_{t,M}$; equation 7).

At any point $B(r_B > r_M)$ beyond the Roche limit the potential energy is a decreasing function of altitude along the field line. A particle with a velocity smaller than

$$V'_M = \sqrt{\psi_M - \psi_B} \tag{12}$$

will not be able to escape out of the equatorial potential well and contributes to the population of the (t_4) class of particles illustrated in panel B of Fig. 1. Besides this new class of low energy particles with reflection points between B and M, there are also trapped particles (t_3), with magnetic mirror points between B and M, and finally the t_2 type with a magnetic mirror between M and the exobase.

The remaining hatched area (e) in panel B corresponds to escaping particles emerging from the ionosphere and flowing through the equatorial plane. Note the absence of ballistic orbits at the point B.

Once all possible orbits or particle classes have been defined at any point A or B, the question is to determine the population or velocity distribution in each region of the velocity space. For the ballistic (b) and escaping (e) particles emerging from the ionosphere it is quite natural to assume that their distribution is the same maxwellian distribution as in the collision dominated region below the exobase

$$f(\mathbf{V}\epsilon\{bUe\})\,d\mathbf{V} = \frac{N_0}{\pi^{3/2}}\,e^{-V^2-\psi}\,dV. \tag{13}$$

If there are no Coulomb or wave–particle interactions between the particles in the exosphere,

one can consider that the velocity distribution of the trapped particles is independent and uncoupled to ballistic particles of ionospheric origin. The usual assumption in the exospheric models of Eviatar *et al.* (1964), Hartle (1969), Lemaire and Scherer (1970) is that

$$f(\mathbf{V}\epsilon\{t_1 U t_2 U t_3 U t_4\}) = 0. \tag{14}$$

It is obvious that these models described ideal conditions where the trapped particles are removed from the flux tube as quickly as they are brought into trapped orbit by collisional deflections. Such conditions are met in the polar wind since the flux tubes are considered as pipes along which the thermal ions can easily escape into the extended magnetotail or magnetosheath. Along "closed" field lines at low and mid-latitudes, convection and cross-L drifts of collisionless plasma elements can also remove trapped particles from a given flux tube. However, unless the trapped particles are continuously pumped away, a flux tube will finally be saturated with thermal trapped particles. Barometric equilibrium is then reached. Any intermediate situation between the exospheric and barometric equilibrium models can be described by adding to the exospheric distribution an appropriate arbitrary distribution of trapped particles with pitch angles outside the loss cone and mirror points above the exobase.

In the following section we calculate the density, the pressure components and total particle content, for these exospheric and barometric models when the rotation speed Ω is arbitrarily taken to be equal to twice Ω_E, the rotation speed of the Earth. Such a large value of Ω is actually observed in the midnight sector outside the plasmasphere.

4. DENSITY DISTRIBUTIONS

4.1

The integration of the Maxwellian velocity distribution (13) over the regions (b) and (e) of the velocity space (panel A, Fig. 1) gives the contribution of the ballistic and escaping particles at the points A or A' inside the Roche limit surface,

$$n_A^{(b,e)} = N_0 e^{-\psi}[1-(1-\eta)^{1/2} e^{-(\eta\psi/1-\eta)}]. \tag{15}$$

The barometric equilibrium density distribution is given by

$$n_A^{(b,e,t_1,t_2)} = N_0 e^{-\psi}. \tag{16}$$

The contribution of the trapped particle to the barometric distribution is

$$n_A^{(t_1,t_2)} = N_0 e^{-\psi}(1-\eta)^{1/2} e^{-(\eta\psi/1-\eta)}, \tag{17}$$

where ψ and η are the dimensionless potential energy and the magnetic field variables defined in the previous section. Since $\psi_{ion} \equiv \psi_{electron}$ for a symmetric and single-ion-exosphere, the same algebraic expressions describe the ion and electron densities. Charge neutrality is therefore satisfied everywhere along the field line when this condition is satisfied at one point, e.g. at the exobase where $n_0^{(b,e)} = N_0$ and $n_0^{(t_1,t_2)} = 0$. Equation (15) is then essentially the same expression as that derived by Eviatar *et al.* (1964) for a non-rotating exosphere.

4.2

The density of the escaping particles (e) at a point B beyond the Roche limit surface is

$$\begin{aligned} n_B^{(e)} = N_0 e^{-\psi}\Big\{ & 1-2K_2(V_M')-(1-\eta)^{1/2} \\ & \times e^{-(\eta\psi/1-\eta)}[1-2K_2(Y_M)] \\ & -(1-\mu)^{1/2}\exp-\left(\frac{\mu(\psi-\psi_M)}{1-\mu}\right) \\ & \times[2K_2(X_M)-2K_2(X_M')]\Big\}, \end{aligned} \tag{18}$$

where V_M' is given by (12)

$$\mu = \frac{\eta}{\eta_M} = \frac{B}{B_M} \tag{19}$$

$$Y_M^2 = \frac{\psi_M}{1-\eta_M} - \frac{\psi}{1-\eta} \tag{20}$$

$$X_M^2 = \frac{\psi_M-\psi}{1-\mu} + \frac{\eta_M\psi_M}{1-\eta_M} \tag{21}$$

$$(X_M')^2 = \frac{\psi_M-\psi}{1-\mu} \tag{22}$$

$K_m(x)$ is a function defined in the Appendix.

The diffusive equilibrium density given by equation (16), has a minimum at $r = r_M$.

The contribution of (t_2) trapped particles with mirror points below the altitude of the potential maximum is

$$\begin{aligned} n_B^{(t_2)} = N_0 e^{-\psi}\Big\{ & (1-\eta)^{1/2} e^{-(\eta\psi/1-\eta)}[1-2K_2(Y_M)] \\ & -(1-\mu)^{1/2}\exp-\left(\frac{\mu(\psi-\psi_M)}{1-\mu}\right)[1-2K_2(X_M)]\Big\}. \end{aligned} \tag{23}$$

The contribution of (t_3) and (t_4) trapped particles with reflection points beyond the Roche limit is

$$n_B^{(t_3,t_4)} = N_0 e^{-\psi}\left\{2K_2(V_M') + (1-\mu)^{1/2} \times \exp - \left(\frac{\mu(\psi-\psi_M)}{1-\mu}\right)[1-2K_2(X_M')]\right\}. \quad (24)$$

For $r_A \to r_0$, $\eta \to 1$, $\psi \to 0$ and $n_A^{(b,e)} \to N_0$, $n_A^{(t_1,t_2)} \to 0$; for $r_B \to r_M$, $\eta \to \eta_M$, $\mu \to 1$, $\psi \to \psi_M$, $V_M' = Y_M' = X_M \to 0$, $n_B^{(t_3,t_4)} \to 0$, $n_B^{(e)}$ and $n_A^{(b,e)}$ have the same limit and the same first derivative at the cross-over point M.

The lowest solid line in Fig. 2 illustrates the relative number density of ballistic and escaping particles along the field line $L = 6$, for $\Omega = 2\Omega_E$ and $T_0 = 3000$ K. Formula (15) is used for $r < r_M = 4.12$ R_E and $|\lambda| > \lambda_M \simeq 34°$. Equation (18) is used for $r > r_M$ and $|\lambda| < \lambda_M$. The lowest dashed line is the result obtained by Eviatar *et al.* (1964) for $\Omega = 0$. It

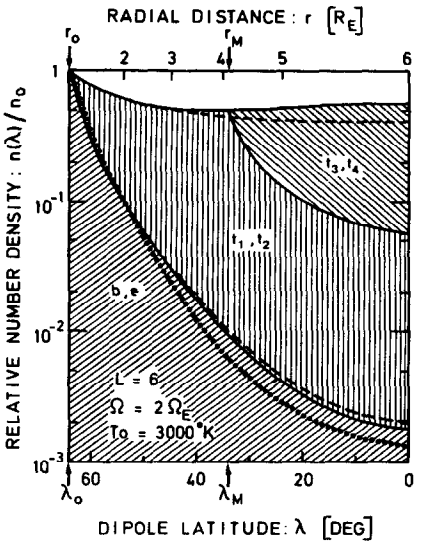

FIG. 2. RELATIVE NUMBER DENSITY ALONG THE FIELD LINE $L = 6$.

The barometric model is represented by the upper curves; the exospheric model without any trapped particles (t_{1-4}) is given by the lower curves; the density distribution in the intermediate exospheric model without trapped particles (t_{3-4}) is also shown. The solid lines illustrate the distribution in an ion-exosphere rotating with an angular velocity equal to twice the rotation speed of the Earth. The corresponding densities in a non-rotating ion-exosphere are shown by the dashed curves. The dotted line refers to the empirical r^{-4} model. The exobase (r_0) is at 1000 km altitude and the exobase temperature is 3000 K for the hydrogen ions and electrons. The maximum of potential energy is at radial distance r_M and latitude λ_M along the field line.

can be seen that an increase of the angular speed Ω decreases the density in an exospheric model near the equatorial plane. The opposite conclusion is true for the barometric equilibrium models illustrated by the upper solid and dashed lines respectively for $\Omega = 2\Omega_E$ and for $\Omega = 0$.

The differently shaded zones in Fig. 2 illustrate the relative importance of the different types of trapped particles. Note that the trapped particles (t_3) and (t_4) constitute 90% of the barometric density in the equatorial plane, while the particles (e) emerging directly from the ionosphere represent only 0.32%.

The dotted line in Fig. 2 corresponds to the r^{-4} empirical model often used in the interpretation of whistler observations (Angerami and Carpenter, 1966).

Figure 3(a) gives the normalized density equatorial distributions for $\Omega = 2\Omega_E$ (solid lines) and for $\Omega = 0$ (dashed lines) when $T_0 = 3000$ K at $r_0 = R_E + 1000$ km. The lowest line corresponds, as in Fig. 2, to the exospheric models; the upper lines refer to the barometric models. Note that the equatorial density, $n(L)$, has a minimum at $L_{FB} = (1.5)^{1/3}L_c$. For $\Omega = \Omega_E$, $L_{FB} = 6.6$; for $\Omega = 2\Omega_E$, $L_{FB} = 4.17$.

The different shadings clearly show that the trapped particles become rapidly predominant in the barometric equatorial density distribution. Note that the L^{-4} density distribution illustrated by the dotted lines is a relatively good approximation for the escaping particles density distribution.

5. PARALLEL AND PERPENDICULAR KINETIC PRESSURES

The parallel and perpendicular pressures are second order moments of the truncated velocity distribution (13–14).

5.1

At any point A inside the Roche limit surface the contributions of the ballistic and escaping particles are

$$P_{\parallel,A}^{(b,e)} = N_0 k T_0 e^{-\psi}[1-(1-\eta)^{3/2}e^{-(\eta\psi/1-\eta)}], \quad (25)$$

$$P_{\perp,A}^{(b,e)} = N_0 k T_0 e^{-\psi}\left\{1-\left(1+\frac{\eta}{2}\right) \times (1-\eta)^{1/2}e^{-(\eta\psi/1-\eta)} - \frac{\eta\psi}{(1-\eta)^{1/2}}e^{-(\eta\psi/1-\eta)}\right\}. \quad (26)$$

In the case of barometric equilibrium (i.e. when the trapped particles are in thermal equilibrium

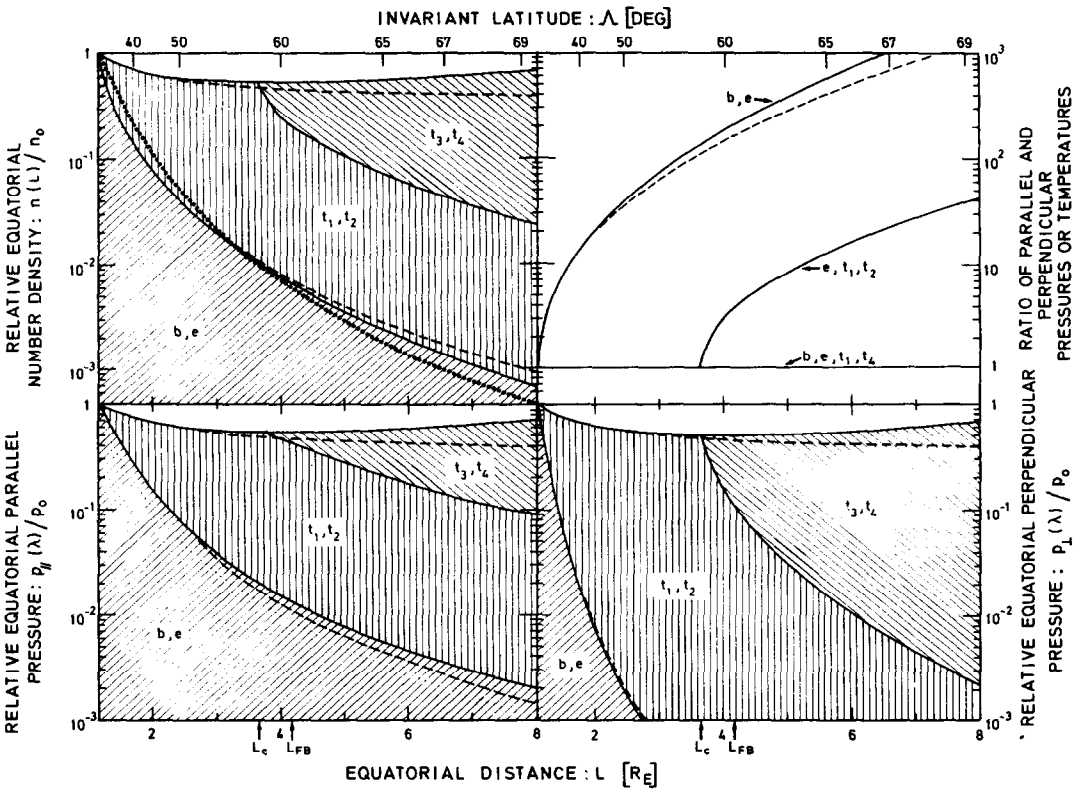

FIG. 3. EQUATORIAL DISTRIBUTIONS. (a) OF THE RELATIVE DENSITY; (b) OF THE RATIO OF PARALLEL AND PERPENDICULAR TEMPERATURE: (c) OF THE RELATIVE PARALLEL PRESSURE: (d) OF THE RELATIVE PERPENDICULAR PRESSURE.

The solid lines correspond to the barometric and exospheric models when the angular velocity equals twice the Earth's rotation speed. The dashed lines refer to non-rotating ion-exospheres. The exobase is at 1000 km altitude and exobase temperature is 3000 K for the hydrogen ions and electrons. L_c is the Roche limit distance in the Earth radii. L_{FB} is the distance where the barometric density distribution has a minimum.

with those emerging from the exobase) the pressure tensor is isotropic and given by

$$P_{\parallel,A}^{(b,e,t_1,t_2)} = P_{\perp,A}^{(b,e,t_1,t_2)} = N_0 kT_0 e^{-\psi}. \tag{27}$$

The pressures due to the trapped particles (t_1) and (t_2) are

$$P_{\parallel,A}^{(t_1,t_2)} = N_0 kT_0 (1-\eta)^{3/2} e^{-(\psi/1-\eta)}, \tag{28}$$

$$P_{\perp,A}^{(t_1,t_2)} = N_0 kT_0 e^{-\psi}\left\{(1-\eta)^{1/2}\left(1+\frac{\eta}{2}\right)e^{-(\eta\psi/1-\eta)} + \frac{\eta\psi}{(1-\eta)^{1/2}} e^{-(\eta\psi/1-\eta)}\right\}. \tag{29}$$

5.2

At any point B beyond the Roche limit the escaping particles have parallel and perpendicular pressures given by:

$$P_{\parallel,B}^{(e)} = N_0 kT_0 e^{-\psi}\{1-\tfrac{4}{3}K_4(V_M') - (1-\eta)^{3/2}e^{-(\eta\psi/1-\eta)}[1-\tfrac{4}{3}K_4(Y_M)] - \tfrac{4}{3}(1-\mu)^{3/2}e^{-(\mu\psi/1-\mu)}[K_4(X_M)-K_4(X_M')]\}, \tag{30}$$

$$P_{\perp,B}^{(e)} = N_0 kT_0 e^{-\psi}\left\{1-\tfrac{4}{3}K_4(V_M') - \left(1+\frac{\eta}{2}\right)(1-\eta)^{1/2}e^{-(\eta\psi/1-\eta)}[1-\tfrac{4}{3}K_4(Y_M)] - \frac{\eta\psi}{(1-\eta)^{1/2}}e^{-(\eta\psi/1-\eta)}[1-2K_2(Y_M)] - \tfrac{4}{3}\left(1+\frac{\mu}{2}\right)(1-\mu)^{1/2}\exp-\left(\frac{\mu(\psi-\psi_M)}{1-\mu}\right)\right.$$

$$\times[K_4(X_M)-K_4(X_M')]-\frac{2\mu(\psi-\psi_M)}{(1-\mu)^{1/2}}$$
$$\times\exp-\left(\frac{\mu(\psi-\psi_M)}{1-\mu}\right)[K_2(X_M)-K_2(X_M')]\Big\}. \quad (31)$$

The barometric equilibrium pressure at the point B is also given by equation (27), and has a minimum at the Roche limit surface, i.e. at $r=r_M$ and $\lambda=\lambda_M$.

The pressures of the trapped particles (t_2) and (t_3, t_4) are

$$P_{\parallel,B}^{(t_2)}=N_0KT_0e^{-\psi}\Big\{(1-\eta)^{3/2}e^{-(\eta\psi/1-\eta)}$$
$$\times[1-\tfrac{4}{3}K_4(Y_M)]-(1-\mu)^{3/2}$$
$$\times\exp-\left(\frac{\mu(\psi-\psi_M)}{1-\mu}\right)[1-\tfrac{4}{3}K_4(X_M)]\Big\}, \quad (32)$$

$$P_{\perp,B}^{(t_2)}=N_0KT_0e^{-\psi}\Big\{\left(1+\frac{\eta}{2}\right)(1-\eta)^{1/2}$$
$$\times e^{-(\eta\psi/1-\eta)}[1-\tfrac{4}{3}K_4(Y_M)]+\frac{\eta\psi}{(1-\eta)^{1/2}}$$
$$\times e^{-(\eta\psi/1-\eta)}[1-2K_2(Y_M)]$$
$$-\left(1+\frac{\mu}{2}\right)(1-\mu)^{1/2}\exp-\left(\frac{\mu(\psi-\psi_M)}{1-\mu}\right)$$
$$\times[1-\tfrac{4}{3}K_4(X_M)]-\frac{\mu(\psi-\psi_M)}{(1-\mu)^{1/2}}$$
$$\times\exp-\left(\frac{\mu(\psi-\psi_M)}{1-\mu}\right)[1-2K_2(X_M)]\Big\}, \quad (33)$$

$$P_{\parallel,B}^{(t_3,t_4)}=N_0KT_0e^{-\psi}\Big\{\tfrac{4}{3}K_4(V_M')$$
$$+(1-\mu)^{3/2}\exp-\left(\frac{\mu(\psi-\psi_M)}{1-\mu}\right)$$
$$\times[1-\tfrac{4}{3}K_4(X_M')]\Big\}, \quad (34)$$

$$P_{\perp,B}^{(t_3,t_4)}=N_0KT_0e^{-\psi}\Big\{\tfrac{4}{3}K_4(V_M')$$
$$+\left(1+\frac{\mu}{2}\right)$$
$$\times(1-\mu)^{1/2}\exp-\left(\frac{\mu(\psi-\psi_M)}{1-\mu}\right)$$
$$\times[1-\tfrac{4}{3}K_4(X_M')]+\frac{\mu(\psi-\psi_M)}{(1-\mu)^{1/2}}$$
$$\times\exp-\left(\frac{\mu(\psi-\psi_M)}{1-\mu}\right)[1-2K_2(X_M')]\Big\}. \quad (35)$$

Figures 3(c) and (d) illustrate the relative equatorial parallel and perpendicular pressure as a function of the equatorial distance. It can be seen that the largest contribution to the pressure tensor is due to the trapped particles when they are present as, for instance, in the barometric equilibrium models. The perpendicular pressure decreases much more rapidly with L than the parallel pressure in all exospheric models. Note that the centrifugal potential increases the parallel pressure but decreases the perpendicular pressure of the escaping particles (compare the lower solid and dashed lines corresponding to $\Omega=2\Omega_E$ and $\Omega=0$, respectively).

Figure 3(b) gives the ratio of parallel to perpendicular pressure or temperatures as a function of the equatorial distance. In the case of barometric equilibrium where the pressure is isotropic, $T_\parallel=T_\perp$. However $T_\parallel$ is larger than $T_\perp$ in all other exospheric models when trapped particles are missing in the velocity distribution.

Figure 4 shows the pressure or temperature ratio as a function of the dipole latitude (lower scale) and radial distance (upper scale) along the field line $L=6$. It can be seen that in the exospheric models $T_\parallel/T_\perp$ increases rapidly with altitude.

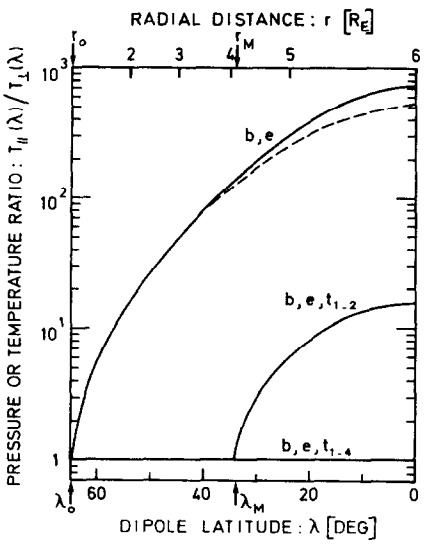

FIG. 4. PRESSURE OR TEMPERATURE RATIO ALONG THE FIELD LINE $L=6$.

The temperature anisotropy is seen to depend drastically on the relative population of trapped particles in the exosphere. The solid curves correspond to rotating ion-exospheres. The dashed line to a non-rotating model. The exobase is at 1000 km, and the exobase temperature is 3000 K for the hydrogen ions and electrons.

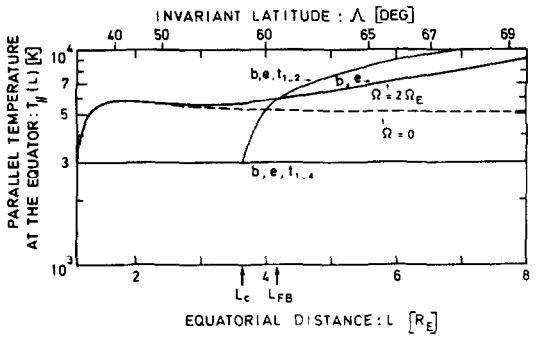

FIG. 5. PARALLEL TEMPERATURE IN THE EQUATORIAL PLANE.

The solid line (b, e) corresponds to the exospheric model without any trapped particles. In the barometric model $T_\parallel$ is equal to the exobase temperature 3000 K. The dashed line refers to the non-rotating model.

Figure 5 shows the parallel temperature in the equatorial plane as a function of L. Note that, in the exospheric model when all trapped particles are missing in the velocity distribution, the equatorial value of $T_\parallel$ increases rapidly from 3000 K (the exobase temperature) to a maximum of 5540 K. Beyond the Roche limit $T_{\parallel,eq}$ is an increasing function of L.

6. TOTAL CONTENTS

In this section we estimate the total amount of mass, kinetic and potential energies stored up in a flux tube of 1 Weber magnetic flux. These quantities are estimated by integration from the altitude of 1000 km to the equator for both hemispheres.

The equatorial section S_{eq} (cm^2) of flux tubes of 1 Weber is given by

$$S_{eq}(L)=\frac{1}{B_{eq}(L)}=3.12\times10^{8}L^{3}\ (\mathrm{cm}^2), \quad (36)$$

and is illustrated as a function of L in Fig. 6(a). Also shown is the ionospheric section S_{1000km} (cm^2) and the volume V (m^3) of these flux tubes.

The total mass, $m_H N_T$ (g) in 1 Weber magnetic flux tubes is given as a function of L for the different exospheric and barometric models considered in the previous sections. When the angular velocity increases, the total mass and particle content in a barometric model increases, while it decreases in the exospheric model, (compare solid and dashed curves in Fig. 6(b) respectively for $\Omega=2\Omega_E$ and $\Omega=0$). It can also be seen that the empirical r^{-4} model predicts values which are different from those of the exospheric model (b, e) by less than 60% for $L<6$.

The total potential energy stored up in a flux tube is defined by

$$\Phi_t(L)=2\int_{r_0}^{r_{eq}} n(r)m[\phi_t(r)-\phi_t(r_0)]S(r)dl, \quad (37)$$

where $r_0=R_E+1000$ km; dl is the element of length along the dipole field line L : $dl=LR\cos\lambda(1+3\sin^2\lambda)^{1/2}$; S is the orthogonal section of the flux tube; $S(\lambda)=S_{eq}\cos^6\lambda(1+3\sin^2\lambda)^{-1/2}$; $m\phi_t$ is the total potential energy defined by equation (5); $n(r)$ is the number density depending on the method considered. The numerical results are displayed in Fig. 6(c) for $T_e=T_p=T_0=3000$ K, $N_0=10^4$ cm^{-3} at the exobase altitude (1000 km), for $\Omega=2\Omega_E$ (solid curves) and $\Omega=0$ (dashed curves); the value of Φ_t is given in J/Wb.

The kinetic energy stored up in a flux tube of 1 Weber is determined by the integral

$$K(L)=2\int_{r_0}^{r_{eq}}\left(\frac{P_\parallel}{2}+P_\perp\right)Sdl, \quad (38)$$

where $P_\parallel$ and $P_\perp$ are the parallel and perpendicular pressures defined in the previous section. The numerical results are shown in Fig. 6(d) where K is displayed in J/Wb.

Since the total potential energy and the pressure of the electron and ions are the same in the single-ion and symmetric exospheric models considered, the values of Φ_t and K calculated by (37) and (38) must be doubled to obtain the total potential energy and kinetic energy of the plasma stored in the whole flux tube.

7. DISCUSSION

The gravitational potential barrier which retains the thermal ionospheric ions close to the Earth, is lowered by the effect of the centrifugal force. For a magnetic field line with L larger than the critical value (6), the total potential energy (5) has a minimum in the equatorial plane.

The plasma beyond the Roche limit surface tends to move outwardly, to pile up near the equatorial plane, and to build up a convectively unstable density distribution for which dn/dr is positive.

The larger the angular speed Ω, the closer to the Earth is the Roche limit and the deeper is the equatorial potential well for a fixed L value. Figures 7(a) and (b) illustrate how the equatorial density, and total particle content of the barometric and exospheric models change at $L=6$ when Ω

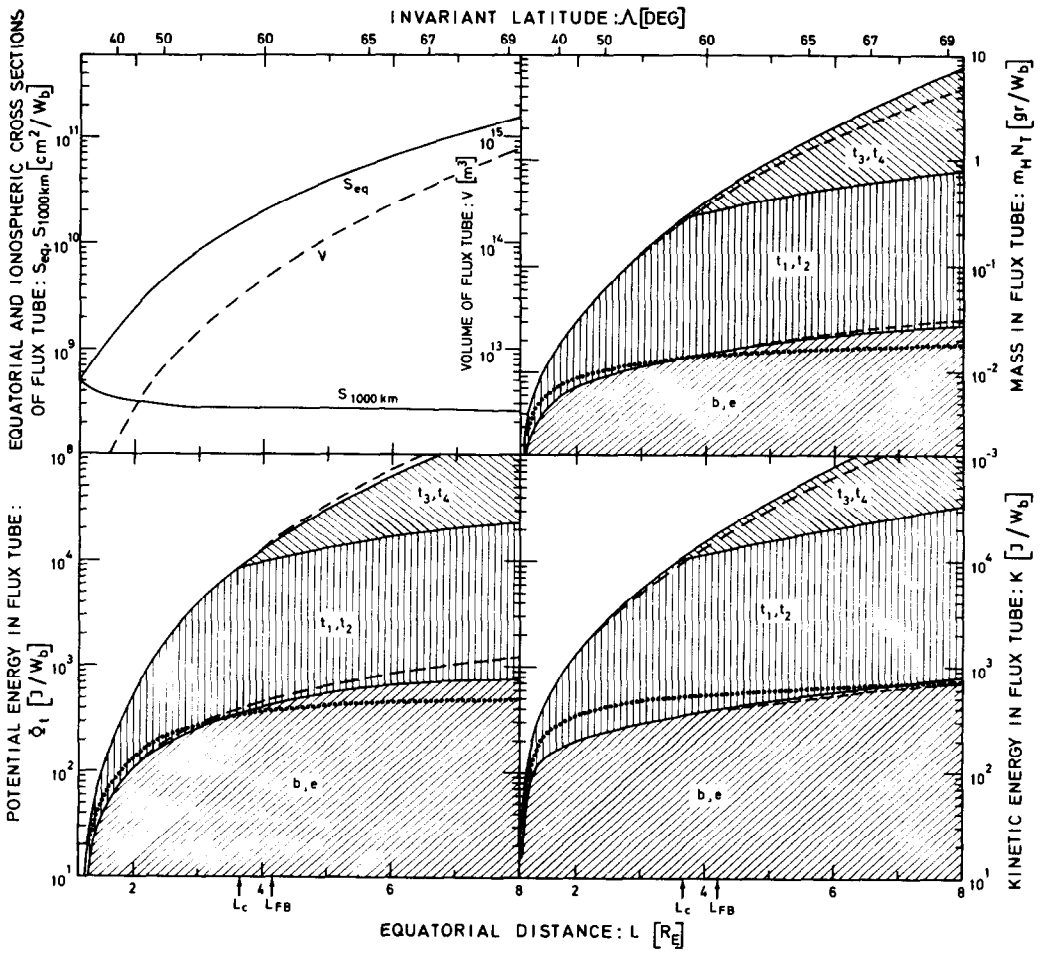

FIG. 6. TOTAL FLUX TUBE CONTENTS.

(a) Total volume, equatorial and exobase (1000 km) sections of 1 Weber magnetic flux tubes as a function of L; (b) total mass in a flux tube for the barometric, the exospheric and the empirical r^{-4} models; (c) total content of potential energy stored up in the hydrogen ions of a 1 Weber flux tube; (d) total content of kinetic energy of the hydrogen ions or electrons confined in a 1 Weber magnetic flux tube above the exobase (1000 km). The exobase temperature and density are respectively 3000 K and 10^4 cm^{-3}. The angular velocity is twice the rotation speed of the Earth (solid lines). The non-rotating models are illustrated by dashed lines.

increases from zero to 10, assuming all other conditions constant, i.e. $T_e = T_{H^+} = 3000$ K and $N_0 = 10^4$ cm^{-3} at 1000 km altitude. It can be seen that the fraction of escaping particles (e) and of trapped particles (t_1, t_2) with mirror points below the Roche limit surface, decrease when Ω increases. However, the equatorial density at $L = 6$ of the trapped particles (t_3, t_4) with mirror points above the Roche limit surface is an increasing function of Ω for $\Omega > 0.95\,\Omega_E$.

The parallel temperature in the equatorial plane at $L = 6$ is also a very sensitive increasing function of Ω in all collisionless models, except for the barometric model. This temperature measures the parallel velocity dispersion. It is significantly higher than the exobase temperature and approximately equal to $T_0\,(1.5+\psi_{eq})/(0.5+\psi_{eq})$ where ψ_{eq} is the equatorial potential energy (equation 9). These exospheric parallel temperatures are comparable to the thermal ion temperatures measured at large radial distances in the plasmasphere, i.e. 5000–10,000 K (Serbu and Maier, 1970; Bezrukikh and Gringauz, 1975). The exospheric parallel temperature is nearly constant along a given field line, except very close to the exobase where it has a sharp gradient.

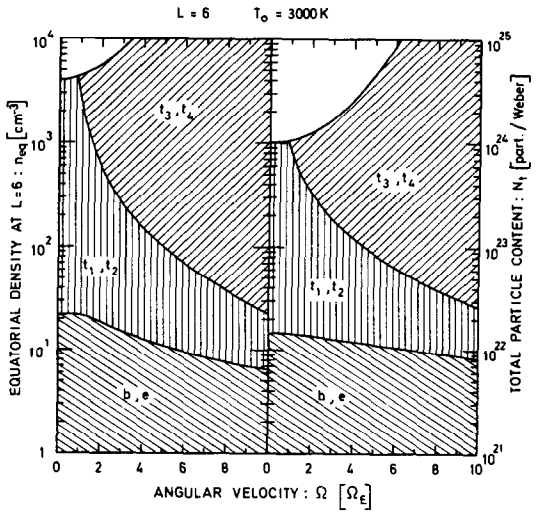

FIG. 7. EQUATORIAL DENSITY (a) AND TOTAL ION CONTENT OF THE 1 Wb MAGNETIC FLUX TUBE AT $L = 6$(b).

The variation of these quantities as a function of the angular velocity of the plasma is illustrated for the barometric, and two exospheric models. The exobase is at 1000 km altitude, the exobase temperature and density are respectively 3000 K and 10^4 cm^{-3}.

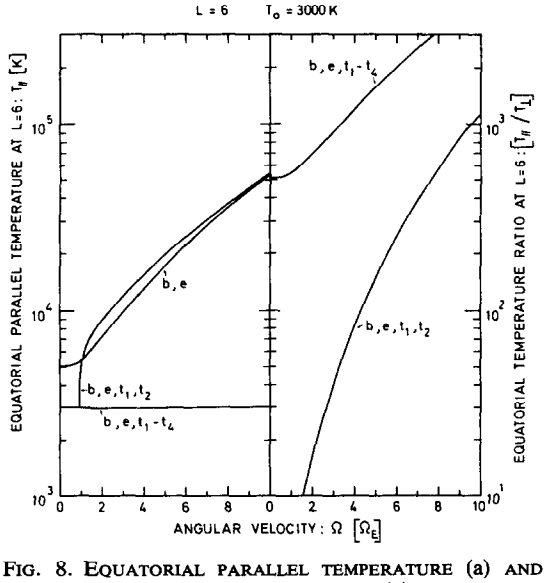

FIG. 8. EQUATORIAL PARALLEL TEMPERATURE (a) AND TEMPERATURE ANISOTROPY (b).

The variation of these quantities as a function of the angular velocity of the plasma is illustrated for the barometric and exospheric models. The exobase is at 1000 km altitude and the exobase temperature is 3000 K. Note the sharp increase with the angular velocity.

Figure 8 shows that the temperature anisotropy in exospheric models is generally large and strongly dependent on the value of Ω, except in the barometric model. A small fraction of trapped particles added to the ballistic and escaping particles velocity distribution can reduce the value of the temperature anisotropy $T_{\parallel}/T_{\perp}$, by a large factor; $T_{\parallel}/T_{\perp}$ is equal to unity only when the trapped particles are in thermal equilibrium with those emerging from the exobase. Since at high altitudes it takes a longer time to achieve the detailed balance equilibrium between the trapped and escaping particles, one can expect large departures from isotropy in the outermost region of the plasmasphere. Indeed when the exobase density suddenly increases the ballistic and escaping particle density will subsequently increase in the exosphere, while the trapped ions especially those with the largest energies and collision times will remain unperturbed for a time comparable to their Coulomb collision time at higher altitudes. During this transient period of time parallel ion temperatures larger than perpendicular ion temperatures should be detected by an instrument with an integration time smaller than 20 seconds.

8. CONCLUSIONS

A collisionless thermal plasma trapped in a dipole magnetic field can be described as a superposition of an exospheric distribution (ballistic and escaping particles) on an arbitrary amount of trapped particles with mirror points above the exobase (where the mean free path is equal to or larger than the scale height). A continuous set of kinetic models can therefore be obtained by changing the trapped particle population from zero to that corresponding to thermal equilibrium (detailed balance between trapped and ballistic escaping particles). The density, temperature and pressure anisotropy in the ion-exosphere depend drastically on the population of trapped particles and on the angular velocity of the cold plasma of ionospheric origin.

As a consequence of the increase of collision time with radial distance in the plasmasphere one can expect large transient departures from thermal equilibrium, from pressure isotropy and from the barometric distribution.

Outside the plasmasphere where the ion Coulomb collision time is of the order of 1–3 hr (in the equatorial plane) the ionospheric plasma distribution along a magnetic field line is expected to resemble the exospheric model with only a small amount of trapped particles.

REFERENCES

Angerami, J. J. and Carpenter D. L. (1966). Whistler studies of the plasmapause in the magnetosphere. 2. Electron density and total tube electron content near the knee in the magnetospheric ionization. *J. geophys. Res.* **71,** 711–725.

Bezrukikh, V. V. and Gringauz, K. I. (1975). Hot zone in the outer Plasmasphere of the Earth. Paper presented at *Symp. on Physics of Plasmapause.* Grenoble, September 1975.

Eviatar, A., Lenchek, A. M. and Singer, S. F. (1964). Distribution of density in an ion-exosphere of a non-rotating planet. *Phys. Fluids* **7,** 1775–1779.

Hartle, R. E. (1969). Ion-exosphere with variable conditions at the baropause. *Phys. Fluids* **12,** 455–462.

Lemaire, J. (1974). The "Roche limit" of ionsopheric plasma and its primary importance for the plasmapause formation. *Planet. Space Sci.* **22,** 757–766.

Lemaire, J. and Scherer, M. (1969). Le champ électrique de polarisation dans l'exosphère ionique polaire, *C.r. Acad. Sci. Paris (B)* **269,** 666–669.

Lemaire, J. and Scherer, M. (1970). Model of the polar ion-exosphere. *Planet. Space Sci.* **18,** 103–120.

Lemaire, J. and Scherer, M. (1971). Kinetic models of the solar wind. *J. geophys. Res.* **76,** 7479–7490.

Lemaire, J. and Scherer, M. (1973a). Kinetic models of the solar and polar winds. *Rev. Geophys. Space Phys.* **11,** 427–468.

Lemaire, J. and Scherer, M. (1973b). Plasmasheet particle precipitation: a kinetic model. *Planet. Space Sci.* **21,** 281–289.

Lemaire, J. and Scherer, M. (1974). Exospheric models of the topside ionosphere. *Space Sci. Rev.* **15,** 591–640.

Melrose, D. B. (1967). Rotational effects on the distribution to thermal plasma in the magnetosphere of Jupiter. *Planet. Space Sci.* **15,** 381–393.

Michel, F. C. and Sturrock, P. A. (1974). Centrifugal instability of the jovian magnetosphere and its interaction with the solar wind. *Planet. Space Sci.* **22,** 1501–1510.

Pannekoek, A. (1922). Ionization in stellar atmospheres. *Bull. Astr. Inst. Neth.* **1,** 107–118.

Rosseland, S. (1924). Electrical state of a star, *Mon. Notic. Roy. Astron. Soc.* **84,** 720–728.

Serbu, G. P. and Maier, E. J. R. (1970). Observations from OGO 5 of the thermal ion density and temperature within the magnetosphere. *J. geophys. Res.* **75,** 6102–6113.

APPENDIX

The Functions $K_m(x)$

The functions $K_m(x)$ are defined by:

$$K_m(x)=\frac{2}{\sqrt{\pi}}\int_0^x \mathrm{d}t\,\exp(-t^2)t^m. \tag{A1}$$

The functions $K_m(x)$ can be expressed in terms of the error function and in terms of exponential function. Indeed, partial integration yields the recurrence formula,

$$K_m(x)=\tfrac{1}{2}(m-1)K_{m-2}(x)-\frac{x^{m-1}}{\sqrt{\pi}}\exp(-x^2), \tag{A2}$$

where straightforward calculation lead to the results

$$K_0(x)=\mathrm{erf}\,(x) \tag{A3}$$

$$K_1(x)=[1-\exp(-x^2)]/\sqrt{\pi}. \tag{A4}$$